Journal of Nuclear Materials 565 (2022) 153770

Contents lists available at ScienceDirect

Journal of Nuclear Materials

journal homepage: www.elsevier.com/locate/jnucmat

Remarkable embrittlement and its origins in quenched reactor pressure vessel steels

Xuejiao Wang[a,*], Wenjiang Qiang[b], Xi Jin[a], Junwei Qiao[a], Yucheng Wu[c], Peter K. Liaw[d]

[a] College of Materials Science and Engineering, Taiyuan University of Technology, Taiyuan 030024, China
[b] School of Materials Science and Engineering, University of Science and Technology Beijing, Beijing 100083, China
[c] National-Local Joint Engineering Research Center of Non-ferrous Metal Materials and Processing Technology, Hefei University of Technology, Hefei 230009, China
[d] Department of Materials Science and Engineering, The University of Tennessee, 2200, Knoxville, TN 37996, USA

ARTICLE INFO

Article history:
Received 10 February 2022
Revised 24 April 2022
Accepted 26 April 2022
Available online 27 April 2022

Keywords:
Reactor pressure vessel steels
Embrittlement
Dislocation networks
Moiré fringes
Thermal stress

ABSTRACT

Reactor pressure vessels (RPVs) are one of the main barriers against nuclear accidents, therefore good toughness is indispensable for keeping the integrity of RPVs to prevent the leakage of radioactive substances. It is well known that high temperature and large thermal gradient of nuclear accidents would lead to embrittlement or even rupture of RPVs. However, how damages originate in severe nuclear accidents is still indistinct. This study is aimed to reveal the embrittlement mechanism under a large temperature gradient in quenched RPV steels. It is found that certain strengthening as well as remarkable embrittlement occurs after quenched, further investigations find it probably derive from the generation of plenty of Moiré fringes and dislocation networks, which are supposed to be generated by shearing of crystal planes. This paper reports the deterioration phenomenon caused by a large thermal gradient, reveals the origins remarkable embrittlement and indicates that extra attention must be aroused to take this thermal-stress-induced embrittlement into consideration in nuclear accidents analysis.

1. Introduction

Nuclear security has constantly attracted public attentions recently, especially since Fukushima nuclear accident. Reactor pressure vessels (RPVs), as one of the main barriers against nuclear accidents, such as loss of coolant accidents (LOCAs) and core melt accidents (CMAs), require an excellent combination of appropriate strength and great toughness to keep its integrity to prevent the leakage of the radioactive substance in reactors [1,2]. Some studies have found that the temperature could reach above 1,000 °C under those accidents, which high temperature and large thermal gradient would lead to embrittlement or even rupture of RPVs [3–6].

It has already been found in dual-phase materials, quenching from high temperature would introduce in the thermal mismatch stress at the interface of the two phases due to their different thermal expansion coefficients. Then dislocations would generate by the release of the thermal mismatch stress [7–9]. However, for RPV steels which is single phase, even though the analyses of thermo-hydraulics, thermo-mechanics and fracture mechanics are conducted to figure out the influence of thermal gradient on the deterioration progress [10–13], unfortunately, how damages originate under high temperature and large thermal gradient and how they evolve subsequently, are still indistinct, which seriously restricts our in-depth understanding about the failure mechanisms of RPVs under extreme nuclear accidents.

This study is aimed to reveal the influence of thermal gradient on mechanical properties of RPV steels and to figure out its deterioration mechanisms.

2. Material and methods

The type of RPV steels utilized was Chinese A508-3 RPV steels and the chemical compositions were listed in Table 1. Raw materials which total weight was 25 kg were melted in a vacuum arc-melting furnace. Then the ingot was forged above 980 °C for 1.5 h to break the dendrites, and cut to bulks with the dimension of 60 × 40 × 150 mm. The initial heat treatment was tempered at 890 °C for 1.5 h and cooled at air (as-received group). Afterwards, to study the influence of quenching, materials were heated at 700 °C for 5 h and then quenched (quenched group). In comparison, materials were heated at 700 °C for 5 h and then air cooled

* Corresponding author.
E-mail address: wangxuejiao@tyut.edu.cn (X. Wang).

https://doi.org/10.1016/j.jnucmat.2022.153770
0022-3115/

Nomenclature

A_1, A_2	energy of the lower platform and upper platform
A_k	impact energy
b	Burgers' vector
D	distance of crystal planes
D_M	distance of Moiré fringes
d	average grain size
d_1, d_2	the interplanar distances of layers
dL/L	linear expansion rate
E	Young's modulus
k_Y	Hall-Petch coefficient
M	Taylor factor
t	temperature
t_0	ductile-to-brittle transition temperature
α	linear coefficient of expansion
α'	constant
γ	surface energy
Δt	a parameter related to the temperature range of the ductile-brittle transition
ΔT	change of temperature
$\Delta\sigma$	strengthening caused by dislocations after quenching
ε	strain
μ	shear modulus
ρ_s	dislocation densities
σ_c	critical stress for crack extension
σ_s	yield strength
σ_{th}	maximum thermal stress
φ	rotation angle of two layers

Acronyms

bcc	body-centered-cube
BF	bright-field
CCT	continuous cooling transformation
CMA	core melt accident
DBTT	ductile-to-brittle transition temperature
DF	dark-field
HRTEM	high-resolution TEM
IFFT	inverse fast Fourier transformation
LOCA	loss of coolant accident
LPE	lower platform
OM	optical microscopy
RPV	reactor pressure vessel
RT	room temperature
SAED	selected area electron diffraction
SEM	scanning electron microscopy
UPE	upper platform
XRD	X-ray diffraction

(air-cooled group). The detailed heat treatments were summarized in Table 2.

Thermal expansion properties were tested on PCY-III high temperature vertical dilatometer utilizing a cylinder sample, whose size was $\phi 10 \times 55$ mm. Tensile tests were conducted by WDW-200D electronic universal material testing machine at room temperature (RT). The accuracy of the loading force and deformation was 0.5% and 1%, respectively, and the displacement rate was 1.6 mm/min. Charpy-V type specimens, whose size was 55 × 10 × 10 mm, were used for impact tests by NI-500 pendulum impact testing machine. The samples analyzed by optical microscopy (OM), scanning electron microscopy (SEM), and X-ray diffraction (XRD) were polished and etched in the 5% (volume fraction) nitric acid. The samples for transmission electron microscopy (TEM) were electro-polished in 10% $HClO_4$ +90% alcohol (volume fraction) at - 25 °C by 20 V.

Table 1
The chemical compositions of RPV steels.

Composition	C	Mn	Si	Ni	Cr	Mo	Fe
Content (wt.%)	0.17	1.27	0.22	0.71	0.098	0.46	Bal

3. Results and discussion

3.1. Microstructures

Fig. 1a presents the XRD patterns of the three groups. Lack of the peak of austenite, it indicates that microstructures of the three groups are all single-phase body-centered-cube (bcc), meaning that austenitizing does not happen in both quenched and air-cooled groups. Moreover, by analyses of OM and SEM, it is found that the microstructures of the three groups are similar. Fig. 1b–c show the microstructures of the as-received group under OM and SEM, respectively. According to the continuous cooling transformation (CCT) curve of RPV steels [14] and the heat treatment listed in Table 2, it could be deduced that the microstructures are needle-like lower bainites - typical microstructures of RPV steels [14,15], consisting of ferrite matrix and isolated banded carbides, between which the angle is around 50°–65°. The results above indicate that the heat preservation at 700 °C does not result in austenitizing, grain coarsening, or extra precipitation of the very steels. Besides, the inset of Fig. 1b shows the thermal-expansion curve of the as-received group, which exhibits that the phase-transformation point of austenitizing is 713 °C, the linear coefficient of expansion, α, is around $16 \times 10^{-6}\ K^{-1}$ above 420 °C, and the linear expansion rate, dL/L is around 1.08% at 700 °C.

3.2. Mechanical properties

Fig. 2a shows the tensile engineering curves of the three groups. It could be found that the tensile curves and tensile properties of as-received group and air cooled group are similar, exhibiting that heat preservation at 700 °C as well as air cooling do not change the mechanical properties of materials. Nevertheless, the yield strength, σ_s, increases from 460 to 540 MPa (17.4%) after quenching. Moreover, the stage of work-hardening of tensile curve vanishes after quenching. Fig. 2b exhibits further analysis on the work-hardening rate, where stage I, II, III means the elastic deformation, the multi-slip, and the cross-slip, respectively. Fig. 2b demonstrates that the quenched group has distinctively a lower work-hardening rate, shorter multi-slip and cross-slip stages, indicating that the slip ability of dislocations decreases remarkably after quenching.

Fig. 2c shows the curves of a series of impact tests, which are fitted by the Boltzmann function

$$A_k = \frac{A_1 - A_2}{1 + e^{(t-t_0)/\Delta t}} + A_2 \quad (1)$$

where A_k is the impact energy, A_1 and A_2 are the energies of the lower platform (LPE) and the upper platform (UPE), respectively, t is the temperature, t_0 is the ductile-to-brittle transition temperature (DBTT), and Δt is a parameter related to the temperature range of the ductile-brittle transition. The results of A_k at RT, UPE, and DBTT of the three groups are presented in Fig. 2d. It could be found that air cooling has less influence on the impact properties, yet remarkable embrittlement occurs after quenching. Specifically, compared with as-received group, A_k at RT of quenched group sharply decreases from 144 to 32 J, UPE sharply decreases from

Table 2
The heat treatment of RPV steels.

Group	Heat treatment
As-received group	initial heat treatment (austenitizing at 890 °C, 1.5 h, cooled at air; then tempered at 650 °C, 6 h, cooled at air)
Quenched group	initial heat treatment + quenched (700 °C*, 5 h, cooled at water)
Air-cooled group	initial heat treatment + normalized (700 °C*, 5 h, cooled at air)

* 700 °C is beneath the austenitizing temperature of 713 °C [shown in Fig. 1a] to prevent phase transition.

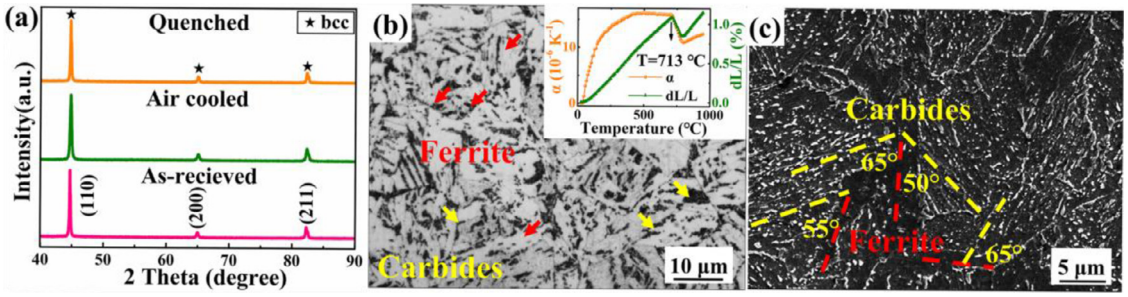

Fig. 1. (a) XRD patterns of the three groups; (b) OM image of the as-received group, the inset is its thermal-expansion curves; (c) SEM image of the as-received group, where the red and yellow lines are the orientations of the long axis of ferrite and carbides, respectively.

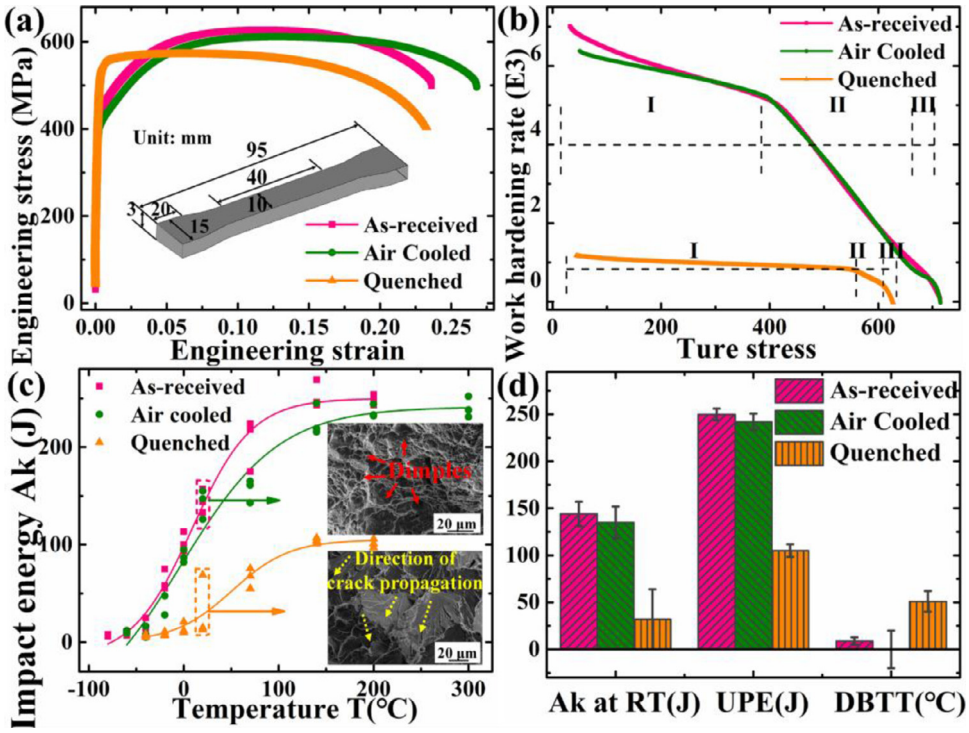

Fig. 2. Mechanical properties of the three groups. (a) the tensile engineering curves; (b) the work-hardening rate curves, where stage I, II, III means the elastic deformation, the multi-slip, and the cross-slip, respectively; (c) the curves of a series impact tests, where the insets are SEM images of the impact fracture of the as-received and quenched groups at RT, respectively; (d) Ak at RT, UPE, and DBTT.

250 to 105 J, and DBTT rapidly increases from 9 to 51 °C. Further investigations on the impact fracture of the as-received and quenched groups at RT are presented in the insets of Fig. 2c, and it shows that the impact fracture transforms from dimple to cleavage after quenching. By analyzing the directions of crack propagation of more than 10 images of quenched group, no crack initiation caused by carbides or precipitates is found, exhibiting that the embrittlement after quenching is not ascribed to the carbides or precipitates, but is supposed to be driven from the thermal stress caused by quenching. Moreover, it is noteworthy that the shift of DBTT (42 °C) after quenching is roughly equivalent to 10^{19} cm^{-2} neutron fluence in most RPV steels, which is around one fifth of the whole lifetime of RPV steels [16–19]. Therefore, it is noteworthy that a large thermal gradient during quenching would result in remarkable embrittlement of RPV steels and threaten the safe operation of the reactors.

3.3. TEM analyses

3.3.1. The microstructures of as-received and air cooled groups

To investigate the embrittlement mechanisms after quenching, TEM analyses of bright-field (BF) and dark-field (DF) on the three groups are conducted. Fig. 3a–d show the microstructures of the as-received and air-cooled groups, respectively. It could be seen that the microstructures of the two groups are similar – both consist of a few of dislocation lines and dislocation tangles, along with

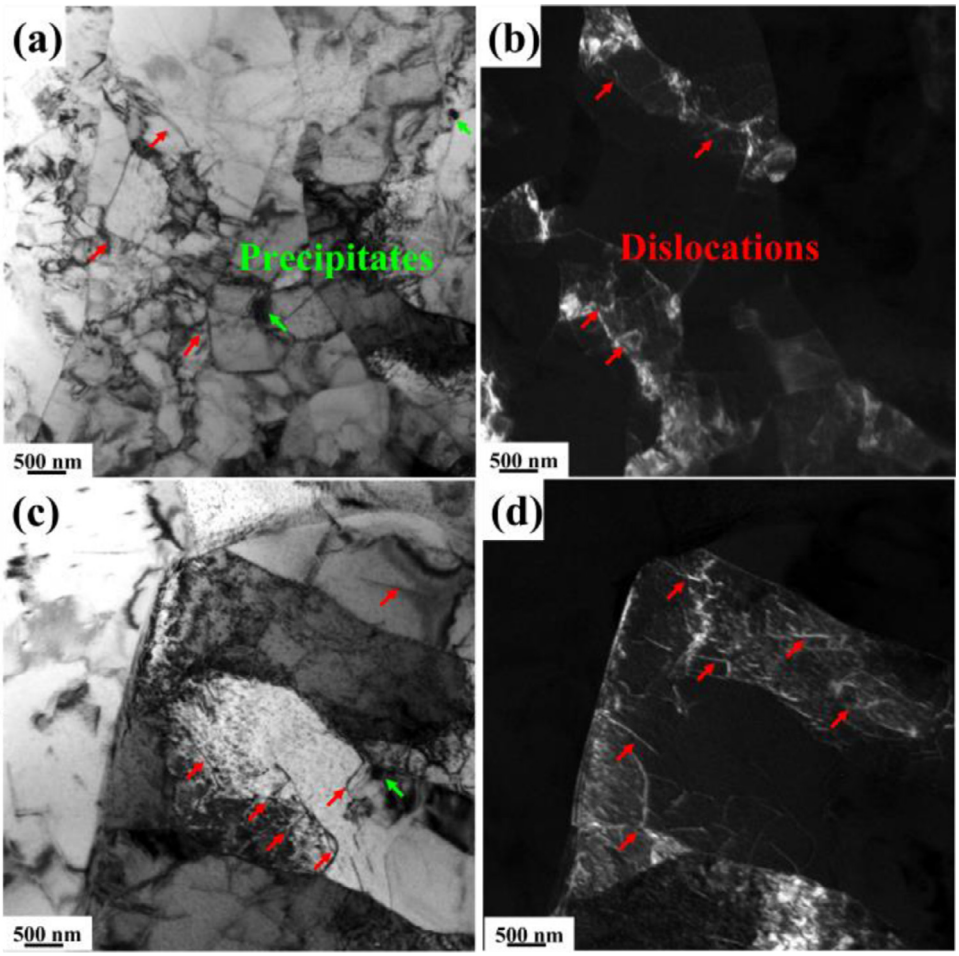

Fig. 3. Microstructures of the as-received (a–b) and air-cooled (c–d) groups under BF and DF modes of TEM.

some precipitates. In contrast, in the quenched group presented in Fig. 4, plenty of regularly arranged Moiré fringes as well as dislocation networks are found, whose distances are 0.4 nm–10 nm and 10 nm–30 nm, respectively. Based on at least 15 TEM pictures, the dislocation densities, ρ_s, of the as-received, air-cooled and quenched groups are roughly estimated by the line intercept method [20] at $(3.4 \pm 1.1) \times 10^{13}$ m^{-2}, $(2.8 \pm 0.8) \times 10^{13}$ m^{-2} and $(2.0 \pm 0.9) \times 10^{14}$ m^{-2}, respectively. It is noteworthy that since some orientations of dislocations are not fully displayed in one diffraction direction, the estimation of ρ_s is somewhat low. Besides, Fig. 4c–d present that the extension of dislocation networks I is obstructed by precipitates, and the sharp corner of dislocation networks I acts as a heterogeneous nucleation site to promote the dislocation nucleation and result in the formation of dislocation networks II.

3.3.2. The Moiré fringes found in quenched group

Moiré fringes are generated by the tilting or rotating of two crystal lattice planes [21]. In many studies, Moiré fringes are usually driven from the discrepancy of lattice parameters between the precipitates and matrix and always found near the interface of the two phases [22–24]. Nevertheless, in this study, Moiré fringes are widely distributed in the matrix of RPV steels, therefore how they generate still needs further investigation. Fig. 5a shows the BF image of Moiré fringes, and its high-resolution TEM (HRTEM) images in Fig. 5b exhibits that the Moiré fringes are overlapped by two lattice planes from the left-bottom and right-top regions, where the distance of the crystal planes, d, and the distance of Moiré fringes, D_M, are 0.082 nm and 0.59 nm, respectively. Further inverse fast Fourier transformation (IFFT) analyses in Fig. 5c–d reveal that the rotation angle between the two lattice planes is around 8°, close to that found in the Fe-Ni-C system (5°) [25]. D_M of rotation Moiré fringes could be calculated by the following equation [21]

$$D_M = \frac{d_1 d_2}{\sqrt{(d_1 - d_2)^2 + d_1 d_2 \varphi^2}} \tag{2}$$

where d_1 and d_2 is the interplanar distances of two layers, respectively, and φ is the rotation angle. When $d_1 = d_2 = d$, it could be simplified to

$$D_M = \frac{d}{\varphi} \tag{3}$$

When $d = 0.082\ nm$ and $\varphi = 8^\circ$, it could be calculated that the theoretical D_M is 0.588 nm, in good agreement with the experimental data (0.59 nm), confirming that Moiré fringes caused by quenching are driven from shearing of two adjacent lattice planes, as illustrated in stage I–III of Fig. 5e.

3.3.3. The dislocation networks found in quenched group

Fig. 6a exhibits the BF image of dislocation networks. According to the selected area electron diffraction (SAED) in Fig. 6b, besides the green set of diffraction spots from the ferrite matrix, there is another set of weak spots and enlarged in Fig. 6c. Further analyses find that the spots are $(\frac{1}{6}\ -\frac{1}{6}\ 1)$ and $(-\frac{1}{6}\ \frac{1}{6}\ 1)$, stretched to 1/4 nm^{-1} in the reciprocal space, and the angle between them is 27°. Subsequent HRTEM analyses in Fig. 6d indicate that the diffraction of those weak spots is driven from crystal planes of $(\frac{1}{6}\ -\frac{1}{6}\ 1)$

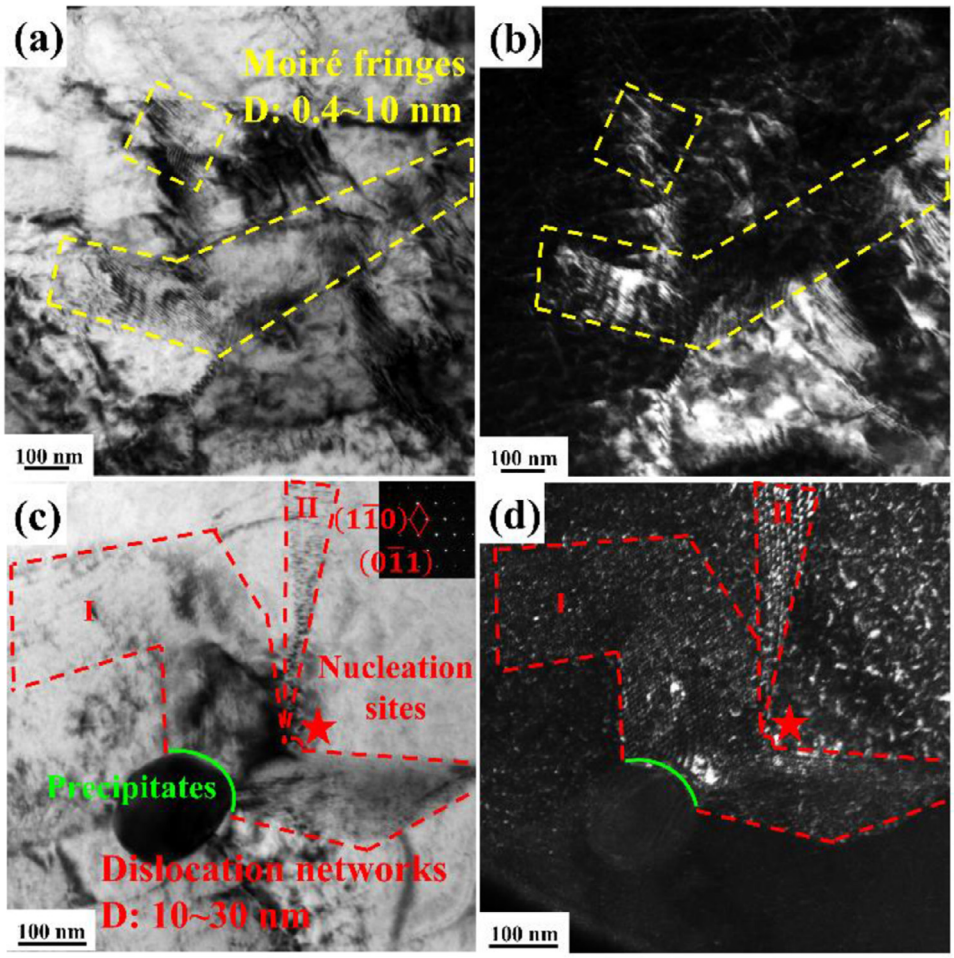

Fig. 4. Moiré fringes (a–b) and dislocation networks (c–d) found in the quenched group, z = [111] in (c–d).

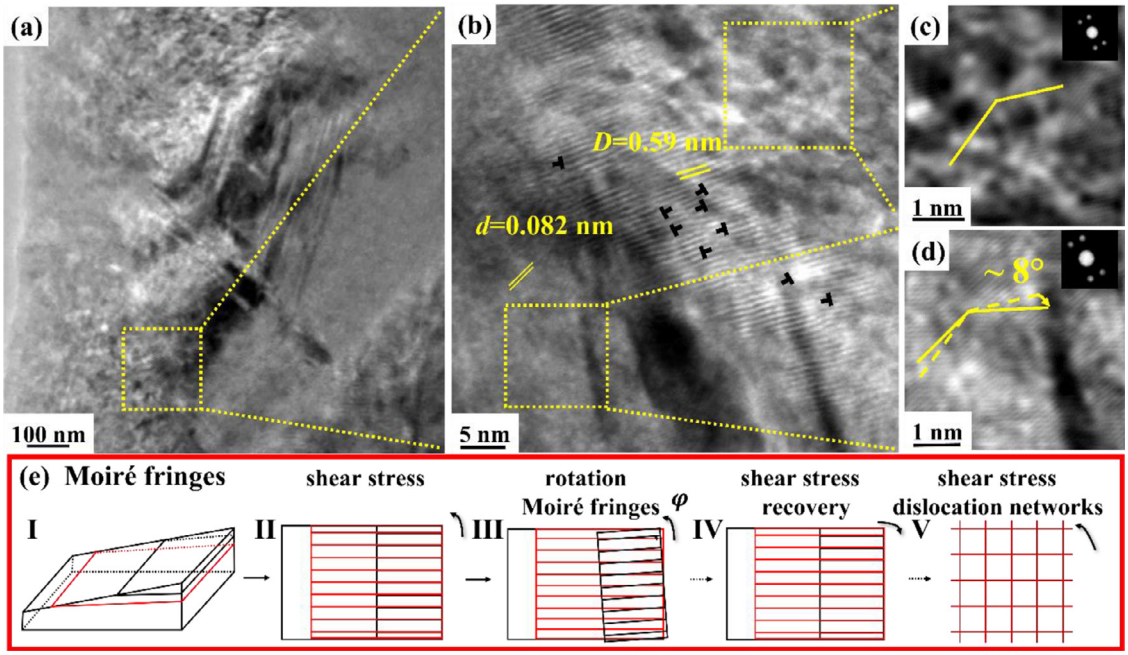

Fig. 5. The TEM images and diagrams of Moiré fringes of the quenched group. (a) BF image of Moiré fringes, (b) HRTEM of (a), (c–d) IFFT of the two regions in (b); (e) diagrams for the formation and evolution of Moiré fringes.

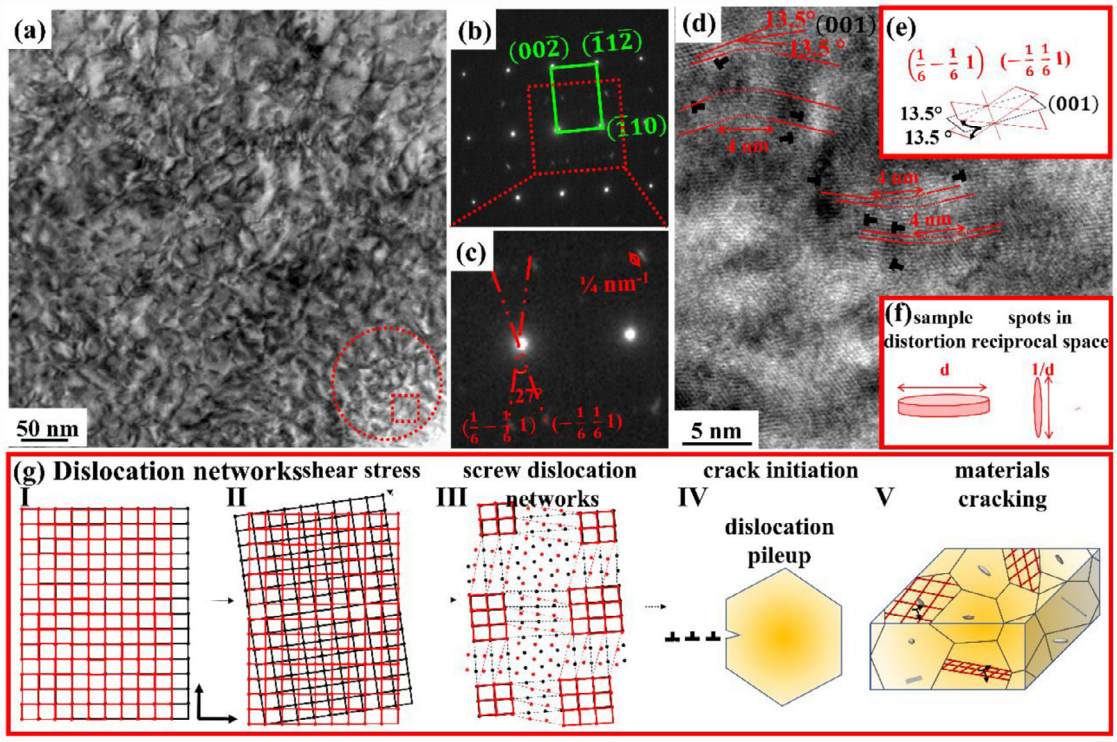

Fig. 6. The TEM images and diagrams of dislocation networks of the quenched group. (a) BF image of dislocation networks; (b–c) SAED of (a), Z=[110]; (d) HRTEM of (c); (e–f) diagrams for (d); (g) diagrams for the formation and evolution of dislocation networks.

and $(-\frac{1}{6}\ \frac{1}{6}\ 1)$, which are generated by the clockwise and anticlockwise rotation of (001) planes for 13.5°, respectively, as illustrated in Fig. 6e. Moreover, the stretching of the spots for 1/4 nm^{-1} in the reciprocal space is driven from a twisted transition region between $(\frac{1}{6}\ -\frac{1}{6}\ 1)$ and $(-\frac{1}{6}\ \frac{1}{6}\ 1)$, where the maximum length in the positive space is around 4 nm, as illustrated in Fig. 6f.

In addition, it is found that the rotation angle of dislocation networks (27°) is larger than Moiré fringes (8°). Therefore, it could be speculated that when external stress is anticlockwise with the rotation angle of Moiré fringes, the rotation angle of Moiré fringes would decrease or even make Moiré fringes disappear, presented in the stage IV of Fig. 5e. On the contrary, when the stress clockwise with the rotation angle is applied, it would increase the rotation angle and make Moiré fringes turn into dislocation networks, presented in the stage V of Fig. 5e.

3.4. The origins of Moiré fringes and dislocation networks

Hereafter, the origins of Moiré fringes and dislocation networks and how they result in strengthening and embrittlement are discussed. The maximum thermal stress, σ_{th}, caused by quenching could be roughly calculated by Hooke's law [26]

$$\sigma_{th} = E\varepsilon \tag{4}$$

where E is Young's modulus, and ε is strain. Given that $E =$ 200 GPa [27], $\varepsilon = 1.08$ % (from RT to 700 °C, RT = 20 °C), it could be calculated that $\sigma_{th} = 2.16$ GPa. It is noteworthy that without consideration of stress relief and plastic deformation, this estimation is very rough and quite overestimated. But it could be deduced that the thermal stress caused by quenching is much higher than the yield strength of RPV steels (460 MPa) and would lead to the plastic deformation of materials, i.e. the multiplication of dislocations. Rather, the shear component of thermal stress would act on adjacent crystal planes and lead to the rotation of adjacent crystal planes. Due to the nonuniformity and polycrystal of materials, in some areas and orientations, dislocations generate due to the rotating of two crystal planes, hence screw dislocation networks are formed, accompanied with some edge dislocations as mismatch, as exhibited in stage I–III of Fig. 6g. In other areas and orientations where dislocations are hard to form, Moiré fringes generate [21], as illustrated in stage I–III of Fig. 5e.

3.5. Mechanisms of strengthening and embrittlement

Strengthening caused by dislocations after quenching, $\Delta\sigma$, could be calculated by:

$$\Delta\sigma = \alpha' M\mu b\left(\sqrt{\rho_{s,after}} - \sqrt{\rho_{s,before}}\right) \tag{5}$$

where α' is constant, ranging from 0 to 1; M is the Taylor factor and equals to 3.06 [28], μ is the shear modulus, b is the Burgers' vector, $\rho_{s,\ as-received}$ and $\rho_{s,\ quenched}$ are the dislocation densities of the as-received and quenched groups, respectively. Given that $\Delta\sigma = 80$ MPa, μ =82.2 GPa [29], b=a=0.286 nm, $\rho_{s,after}$=2×10^{14} m^{-2}, $\rho_{s,\ before}$=3×10^{13} m^{-2}, it could be calculated that α' equals to 0.128, lower than α' of dislocations caused by cold rolling ($\alpha' = 0.4$) [30] and α' of dislocation loops caused by irradiation ($\alpha' = 0.3$) [29,31]. This is probably because that screw dislocations could slip and cross slip more easily than edge dislocations and dislocation loops, the weak hindrance of screw dislocation slipping results in a lower work-hardening rate and earlier cross slipping of quenched RPV steels, as exhibited in Fig. 2b.

Regularly arranged dislocation networks contain many identical dislocations, and they would pile up when stress is applied, hence promote the nucleation and growth of cracks, as shown in stage IV of Fig. 6g. The critical stress for crack extension, σ_c, could be calculated by [32]:

$$\sigma_c = \frac{2\mu\gamma}{k_Y\sqrt{d}} \tag{6}$$

where γ is the surface energy, k_Y is the Hall-Petch coefficient, and d is the average grain size. The rotation of adjacent crystal planes would lower the surface energy of crystal planes and decrease the critical stress for crack extension. Both the nucleation and growth of cracks, as well as the decrease of surface energy would raise the risk for cracking and lead to the embrittlement of materials.

4. Conclusions

Remarkable embrittlement is found in RPV steels quenched beneath the austenitizing temperature, not accompanied with austenitizing, grain coarsening, or extra precipitation. Further investigations have found that the remarkable embrittlement is ascribed to the formation of Moiré fringes and dislocation networks, which is deduced to be generated by the rotation of lattice planes under the shear component of thermal stress during quenching. The dislocation networks would promote the nucleation and growth of cracks, decrease the surface energy for crack extension, hence raise the risk for cracking and lead to the embrittlement of RPV steels. This study illustrates that extra attention should be paid to take the quenching-induced embrittlement into consideration in severe nuclear accidents analysis.

Declaration of Competing Interest

The authors declare that they have no known competing financial interests or personal relationships that could have appeared to influence the work reported in this paper.

CRediT authorship contribution statement

Xuejiao Wang: Conceptualization, Methodology, Validation, Formal analysis, Investigation, Writing – original draft, Writing – review & editing, Visualization, Supervision. **Wenjiang Qiang:** Conceptualization, Methodology, Resources, Funding acquisition. **Xi Jin:** Methodology, Formal analysis, Writing – review & editing. **Junwei Qiao:** Conceptualization, Formal analysis, Writing – original draft, Writing – review & editing, Visualization. **Yucheng Wu:** Methodology, Writing – original draft, Writing – review & editing. **Peter K. Liaw:** Writing – review & editing, Visualization.

Acknowledgments

The work was supported by the Natural Science Foundation of Shanxi Province, China (No. 20210302124043), the National Key Research and Development Program of China (No. 2019YFE03120002), the National Natural Science Foundation of China (Nos. 52020105014, 51828101), the National Science Foundation (DMR-1611180, 1809640). And the authors were very thankful to the dedicated help of teacher Chenghua Li at materials testing center of University of Science and Technology Beijing with the mechanical tests.

References

[1] S.J. Zinkle, G.S. Was, Materials challenges in nuclear energy, Acta Mater. 61 (2013) 735–758, doi:10.1016/j.actamat.2012.11.004.
[2] G.R. Odette, T. Yamamoto, T.J. Williams, R.K. Nanstad, C.A. English, On the history and status of reactor pressure vessel steel ductile to brittle transition temperature shift prediction models, J. Nucl. Mater. 526 (2019) 151863, doi:10.1016/j.jnucmat.2019.151863.
[3] D. Zhan, F. Liu, X. Zhang, H. Chen, J. Li, Ablation and thermal stress analysis of RPV vessel under heating by core melt, Nucl. Eng. Des. 330 (2018) 550–558, doi:10.1016/j.nucengdes.2018.02.008.
[4] M.A. Amidu, Y. Addad, J.I. Lee, D.H. Kam, Y.H. Jeong, Investigation of the pressure vessel lower head potential failure under IVR-ERVC condition during a severe accident scenario in APR1400 reactors, Nucl. Eng. Des. 376 (2021) 111107, doi:10.1016/j.nucengdes.2021.111107.
[5] Z. Li, H. Chang, F. Fang, K. Han, L. Chen, B. Hao, Investigation of water injection on molten zirconium-stainless steel pool in IVR strategy, Ann. Nucl. Energy 161 (2021) 108475, doi:10.1016/j.anucene.2021.108475.
[6] C. Lu, X. Wu, Y. He, Z. Gao, R. Liu, Z. Chen, W. Zheng, J. Yang, Deformation mechanism-based true-stress creep model for SA508 Gr.3 steel over the temperature range of 450–750 °C, J. Nucl. Mater. 526 (2019) 151776, doi:10.1016/j.jnucmat.2019.151776.
[7] Y.W. Chen, B.M. Huang, Y.T. Tsai, S.P. Tsai, C.Y. Chen, J.R. Yang, Microstructural evolutions of low carbon Nb/Mo-containing bainitic steels during high-temperature tempering, Mater. Charact. 131 (2017) 298–305, doi:10.1016/j.matchar.2017.07.022.
[8] K. Hagihara, Y. Hama, K. Yuge, T. Nakano, Misfit strain affecting the lamellar microstructure in $NbSi_2$/$MoSi_2$ duplex crystals, Acta Mater. 61 (2013) 3432–3444, doi:10.1016/j.actamat.2013.02.035.
[9] Z.W. Zhang, C.T. Liu, X.L. Wang, M.K. Miller, D. Ma, G. Chen, J.R. Williams, B.A. Chin, Effects of proton irradiation on nanocluster precipitation in ferritic steel containing fcc alloying additions, Acta Mater. 60 (2012) 3034–3046, doi:10.1016/j.actamat.2012.02.008.
[10] D.F. Mora, M. Niffenegger, G. Qian, M. Jaros, B. Niceno, Modelling of reactor pressure vessel subjected to pressurized thermal shock using 3D-XFEM, Nucl. Eng. Des. 353 (2019) 110237, doi:10.1016/j.nucengdes.2019.110237.
[11] K. Thamaraiselvi, S. Vishnuvardhan, Fracture studies on reactor pressure vessel subjected to pressurised thermal shock: a review, Nucl. Eng. Des. 360 (2020) 110471, doi:10.1016/j.nucengdes.2019.110471.
[12] D.F. Mora, O.C. Garrido, R. Mukin, M. Niffenegger, Fracture mechanics analyses of a reactor pressure vessel under non-uniform cooling with a combined TRACE-XFEM approach, Eng. Fract. Mech. 238 (2020) 107258, doi:10.1016/j.engfracmech.2020.107258.
[13] F.J. Tsai, M. Lee, H.C. Liu, Simulation of the in-vessel retention device heat-removal capability of AP-1000 during a core meltdown accident, Ann. Nucl. Energy 99 (2017) 455–463, doi:10.1016/j.anucene.2016.09.052.
[14] B. Marini, X. Averty, P. Widient, P. Forget, F. Barcelo, Effect of the bainitic and martensitic microstructures on the hardening and embrittlement under neutron irradiation of a reactor pressure vessel steel, J. Nucl. Mater. 465 (2015) 20–27, doi:10.1016/j.jnucmat.2015.05.023.
[15] C. Xie, Z. Liu, X. Wang, X. He, S. Qiao, Effect of two-step tempering treatment on microstructure and impact toughness of bainitic steel for heavy wall thickness reactor pressure vessels, Mater. Charact. 160 (2020) 110070, doi:10.1016/j.matchar.2019.110070.
[16] K. Hata, H. Takamizawa, T. Hojo, K. Ebihara, Y. Nishiyama, Y. Nagai, Grain-boundary phosphorus segregation in highly neutron-irradiated reactor pressure vessel steels and its effect on irradiation embrittlement, J. Nucl. Mater. 543 (2021) 152564, doi:10.1016/j.jnucmat.2020.152564.
[17] G.R. Odette, On the dominant mechanism of irradiation embrittlement of reactor pressure vessel steels, Scr. Metall. 17 (1983) 1183–1188, doi:10.1016/0036-9748(83)90280-6.
[18] Y. Nishiyama, K. Onizawa, M. Suzuki, J.W. Anderegg, Y. Nagai, T. Toyama, M. Hasegawa, J. Kameda, Effects of neutron-irradiation-induced intergranular phosphorus segregation and hardening on embrittlement in reactor pressure vessel steels, Acta Mater. 56 (2008) 4510–4521, doi:10.1016/j.actamat.2008.05.026.
[19] K. Fukuya, Current understanding of radiation-induced degradation in light water reactor structural materials, J. Nucl. Sci. Technol. 50 (2013) 213–254, doi:10.1080/00223131.2013.772448.
[20] R.K. Ham, The determination of dislocation densities in thin films, Philos. Mag. 6 (1961) 1183–1184, doi:10.1080/14786436108239679.
[21] R. by P.D. Brown, Transmission Electron Microscopy-A Textbook for Materials Science, by David B. Williams and C. Barry Carter Springer, 1999, doi:10.1017/s1431927699990529.
[22] D. Poddar, P. Cizek, H. Beladi, P.D. Hodgson, The evolution of microbands and their interaction with NbC precipitates during hot deformation of a Fe-30Ni-Nb model austenitic steel, Acta Mater. 99 (2015) 347–362, doi:10.1016/j.actamat.2015.08.003.
[23] J.H. Rao, Y. Zhang, K. Zhang, A. Huang, C.H.J. Davies, X. Wu, Multiple precipitation pathways in an Al-7Si-0.6Mg alloy fabricated by selective laser melting, Scr. Mater. 160 (2019) 66–69, doi:10.1016/j.scriptamat.2018.09.045.
[24] X.L. Li, X.T. Deng, C.S. Lei, Z.D. Wang, New orientation relationship with low interfacial energy in MC/ferrite system observed in Nb-Ti bearing steel during isothermal quenching process, Scr. Mater. 163 (2019) 101–106, doi:10.1016/j.scriptamat.2019.01.008.
[25] L.W. Yin, M. Sen Li, Z. Da Zou, Z.G. Gong, Z.Y. Hao, Prismatic dislocation loops and concentric dislocation loops in HPHT-grown diamond single crystals, Mater. Sci. Eng. A. 343 (2003) 158–162, doi:10.1016/S0921-5093(02)00385-4.
[26] J.P. Mathieu, K. Ishihara, S. Berveiller, O. Diard, A micromechanical interpretation of the temperature dependence of Beremin model parameters for french RPV steel, J. Nucl. Mater 406 (2010) 97–112, doi:10.1016/j.jnucmat.2010.02.025.
[27] P. Forget, B. Marini, L. Vincent, Application of local approach to fracture of an RPV steel: Effect of the crystal plasticity on the critical carbide size, Procedia Struct. Integr. 2 (2016) 1660–1667, doi:10.1016/j.prostr.2016.06.210.
[28] R.E. Stoller, S.J. Zinkle, On the relationship between uniaxial yield strength and resolved shear stress in polycrystalline materials, J. Nucl. Mater. 283–287 (2000) 349–352, doi:10.1016/S0022-3115(00)00378-0.
[29] F. Bergner, F. Gillemot, M. Hernández-Mayoral, M. Serrano, G. Török, A. Ulbricht, E. Altstadt, Contributions of Cu-rich clusters, dislocation loops and

nanovoids to the irradiation-induced hardening of Cu-bearing low-Ni reactor pressure vessel steels, J. Nucl. Mater. 461 (2015) 37–44, doi:10.1016/j.jnucmat.2015.02.031.

[30] K. Yaegashi, Evaluation of dislocation structure in tensile and fatigue deformed steels by magnetic measurement, ISIJ Int. 48 (2008) 461–466, doi:10.2355/isijinternational.48.461.

[31] F. Bergner, C. Pareige, M. Hernández-Mayoral, L. Malerba, C. Heintze, Application of a three-feature dispersed-barrier hardening model to neutron-irradiated Fe-Cr model alloys, J. Nucl. Mater. 448 (2014) 96–102, doi:10.1016/j.jnucmat.2014.01.024.

[32] L. Wang, T. Shandong, Strengthening and Toughening of Materials, Shanghai Jiao Tong University Press, 2012.